Journal of Geophysical Research: Space Physics

RESEARCH ARTICLE
10.1029/2017JA025001

Key Points:
- Two-mode ionospheric disturbances are found from GPS TEC following the 2005 NC earthquake
- The slow mode disturbance is the acoustic wave induced by the fault rupture in focal regions
- The fast mode disturbance is more likely secondary vertical acoustic wave triggered by the Rayleigh wave

Correspondence to:
S. Jin,
sgjin@nuist.edu.cn;
sg.jin@yahoo.com

Citation:
Jin, S. (2018). Two-mode ionospheric disturbances following the 2005 Northern California offshore earthquake from GPS measurements. *Journal of Geophysical Research: Space Physics*, *123*, 8587–8598. https://doi.org/10.1029/2017JA025001

Received 11 NOV 2017
Accepted 19 AUG 2018
Accepted article online 27 AUG 2018
Published online 3 OCT 2018

Two-Mode Ionospheric Disturbances Following the 2005 Northern California Offshore Earthquake From GPS Measurements

Shuanggen Jin[1,2]

[1]School of Remote Sensing and Geomatics Engineering, Nanjing University of Information Science and Technology, Nanjing, China, [2]Shanghai Astronomical Observatory, Chinese Academy of Sciences, Shanghai, China

Abstract Seismo-ionospheric anomalies have been reported, while its disturbance modes, patterns, and mechanism are very complex for different kinds of earthquakes. The earthquake with M_w = 7.2 occurred off the coast of Northern California with strike-slip faulting on 15 June 2005, which may provide a new insight on ionospheric disturbance waves and patterns from dense Global Positioning System (GPS) observations. In this paper, the detailed seismic ionospheric disturbance modes and characteristics are investigated from dense GPS observations following the 2005 Northern California offshore earthquake. Around 10 min after the earthquake, significant ionospheric disturbances are observed by GPS total electron content (TEC). Furthermore, two-mode ionospheric disturbances are clearly found with two speeds, 1.51 and 2.31 km/s. The slow-propagating mode has an amplitude of 0.02–0.04 total electron content unit (TECU), while the fast-propagating mode has an amplitude of 0.1–0.2 TECU. The frequency spectrogram of the slow mode is around 3.7 mHz, while typical frequency of the fast mode is about 5.3 mHz. The fast-propagating mode is close to the speed of the seismic Rayleigh wave, which is the up propagating secondary acoustic wave triggered by the Rayleigh wave. The slow mode ionospheric disturbance is propagating horizontally as the acoustic wave at the ionospheric level, which is caused by the fault rupture in focal regions.

1. Introduction

Ionospheric disturbances could be excited by various natural or artificial events from the Earth's interior to the top of the atmosphere, such as volcanoes, earthquakes, and geomagnetic storms (Afraimovich et al., 2010, 2013; Aoyama et al., 2016; Dautermann et al., 2009; Grawe & Makela, 2016; Jin et al., 2007; Jin & Park, 2007). These natural events excite acoustic resonance between the Earth's surface and the atmosphere. Some of the resonance waves leak upward into the ionosphere and then trigger ionospheric disturbances (Shinagawa et al., 2007). Nowadays, Global Positioning System (GPS) can estimate atmospheric delays (Jin et al., 2004, 2006, 2016), which can be used to monitor atmospheric and ionospheric disturbances (Catherine et al., 2017; Jin et al., 2011). Seismic ionospheric disturbance (SID) is one of the most important ways to study and understand the interaction and coupling of solid Earth and the ionosphere. Although it is still very challenging to understand the mechanism and electrodynamic-atmospheric interactions in different Earth's layers following the earthquake, the earthquake-induced ionospheric anomalies can be monitored by GPS total electron content (TEC) (e.g., Jin et al., 2015; Jin, Jin, & Kutoglu, 2017; Rolland et al., 2013). Comparing to traditional ionospheric monitoring techniques, for example, incoherent scatter radars and ionosondes, GPS can obtain near-real-time ionospheric TEC with high precision and high temporal resolution as well as all-weather observations, which has been widely used to monitor seismic ionospheric perturbations and study its variation characteristics since 1990s (Calais & Minster, 1995).

The ionospheric disturbance triggered by great earthquakes can be observed as ionospheric TEC anomalies (Heki et al., 2006; Liu et al., 2006). GPS is a powerful tool to observe the atmospheric or ionospheric response to the earthquakes, particularly for areas with dense continuous operating GPS stations. For example, the GPS TEC anomalies following the 2004 great Sumatra earthquake were found and known as an *N*-shaped disturbance (Heki et al., 2006). Later the TEC disturbances following earthquakes were found to be more complicated and have different modes with different features. For example, the seismic ionospheric perturbations following the great 2004 Sumatra earthquake were observed with the direct acoustic wave from the

epicenter area, the secondary acoustic wave caused by the far-field Rayleigh wave, and the gravity wave induced by tsunami (Heki et al., 2006; Jin et al., 2015). The results of the 2011 Tohoku earthquake in Japan also confirmed seismic ionospheric perturbations with three different propagation speeds, namely, the acoustic waves (0.3–1.5 km/s), seismic Rayleigh waves (2–3 km/s), and tsunami generated gravity waves (0.1–0.3 km/s) (Jin et al., 2015; Rolland et al., 2011; Saito et al., 2011).

The features of seismic-ionospheric TEC anomalies were closely associated with the intensity and type of the earthquake. For example, the amplitude of the TEC disturbances was thought to be influenced by the distance between the epicenter and the background TEC. The TEC anomalies triggered by the vertical crustal displacement have been widely analyzed, while the strike-slip earthquake can also excite ionospheric disturbance (Astafyeva et al., 2014), which can cause TEC anomalies with smaller amplitude compared with vertical crustal motion earthquakes. Despite of the amplitude, the waveform of the variations was more or less depended on the focal mechanisms. For example, Afraimovich et al. (2010) found strong *N*-shaped acoustic waves following the 2008 Wenchuan earthquake with a plane waveform. The features of seismo-ionospheric disturbances including velocities, propagating direction, and amplitude of the ionospheric anomalies triggered by great earthquakes were further studied (Jin et al., 2014; Vukovic & Kos, 2017), but the disturbance mode and the coupling between the earthquake and the ionosphere are still not clear. Understanding disturbance characteristics and the coupling process will contribute to a comprehensive knowledge of the procedure and the mechanism of earthquakes, and help human to mitigate the damage. However, the characteristics and behaviors of seismic ionospheric perturbations vary with the earthquake fault type, depth, and focal mechanism.

The 2005 $M_w = 7.2$ earthquake occurred off the coast of Northern California with strike-slip faulting and 10 km in depth at 02:50:54 (UT), 15 June 2005, about 146 km West of Crescent City, CA, in the middle of the Gorda Plate to the west of the Cascadia subduction zone. This earthquake was widely felt along the Northern California-southern Oregon coast line. The motion with the NE striking strike-slip fault is similar to other sequences that have occurred in this region in the past. This strike-slip faulting earthquake with dense GPS observations operated by the University NAVSTAR Consortium (UNAVCO) may provide a new chance to monitor and understand seismic ionospheric disturbance characteristics and modes. In this paper, the seismic ionospheric disturbances are estimated following the 2005 Northern California offshore earthquake from the dense GPS measurements, and the features of the ionospheric perturbation mode are further studied and discussed as well as possible mechanisms. In section 2, data and methods are introduced, results and discussions are presented in section 3, and finally, summary is given in section 4.

2. Data and Methods

It is well known that the ionospheric refraction will affect the propagation of the electromagnetic wave, when it propagates into the Earth's ionosphere. The magnitude of GPS signal code delay and phase advance in the Earth's ionosphere is related to the ionospheric electron density on the raypath and the carrier frequency. Using dual-frequency GPS observations, the precise ionospheric TEC could be extracted from combining code-phase measurements with ignoring the high-order ionospheric effects as (Brunini & Azpilicueta, 2009; Jin et al., 2014; Jin, Jin, & Li, 2017):

$$\begin{aligned} \mathrm{TEC} &= \frac{{f_1}^2 {f_2}^2}{40.28\left({f_1}^2 - {f_2}^2\right)}[L_1 - L_2 + \lambda_1(N_1 + b_1) - \lambda_2(N_2 + b_2) + \varepsilon_L] \\ &= \frac{{f_1}^2 {f_2}^2}{40.28\left({f_2}^2 - {f_1}^2\right)}[P_1 - P_2 - (d_1 - d_2) + \varepsilon_P] \end{aligned} \tag{1}$$

where TEC is the total electron content, L_1 and L_2 are the GPS phase measurements, P_1 and P_2 are the GPS code measurements, N is the ambiguity, f_1 and f_2 are the frequency of GPS (f_1 = 1,575.42 MHz, f_2 = 1,227.60 MHz), d_1 and d_2 are the differential code biases, and ε is the residual. In order to estimate the temporal-spatial distribution of seismo-ionospheric disturbances, the slant TEC along the GPS line of sight (LOS) is converted into the vertical TEC (*vTEC*) using the mapping function as

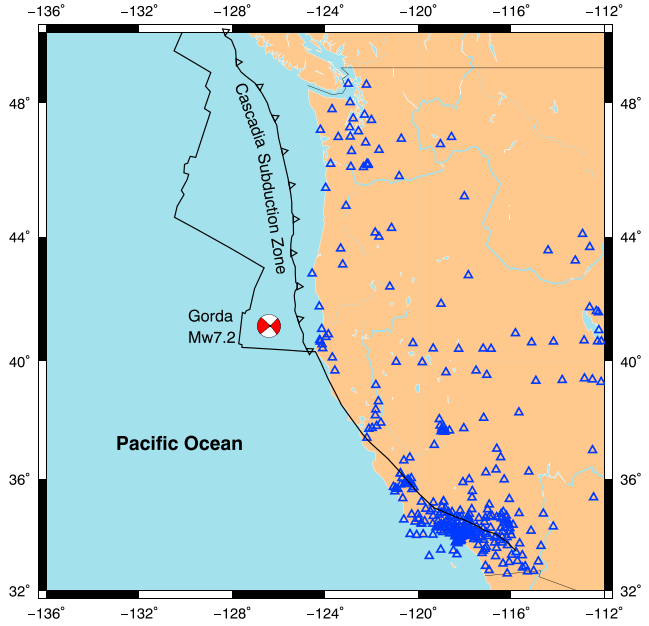

Figure 1. The distribution of GPS stations with the epicenter location in pentagram.

$$vTEC = TEC^{*} \cos\left[\arcsin\left(\frac{R\sin z}{R+H}\right)\right] \quad (2)$$

where H is the thin shell height of the ionosphere (here H is set as 300 km), R is the Earth's radius, and z is the zenith distance of the line of sight (LOS) from the receiver to GPS satellites. The points at the thin shell are referred to as ionospheric piercing points (IPP). The precise *vTEC* can be obtained using code-smoothing phase measurements, while ambiguity, differential code biases, and noises are estimated as constant (e.g., Jin, Jin, & Kutoglu, 2017). For seismic ionospheric disturbances, it is important to obtain the relative ionospheric variations following the earthquake rather than the magnitude of absolute TEC, so here the relative TEC time series are obtained from high-precision GPS carrier phase observations. The constant terms are removed by a low-frequency filtering, for example, instrument deviations and ambiguities of GPS carrier phase observations. In addition, cycle slips of GPS measurements are detected and repaired using the ionospheric residual method of time-difference phase observations and TurboEdit algorithm (Blewitt, 1990). In order to get the obvious seismic ionospheric perturbations, the background TEC variations are removed using the Butterworth filter of a fourth-order zero-phase finite impulse. Since the acoustic cutoff frequency is 3 mHz at above 150-km altitudes and the Nyquist frequency is about 7 mHz for GPS observations with the sampling interval of normally less than 60 s, the passband is set from 3 to 7 mHz (less than the Nyquist frequency). Here 504 stations of continuous GPS measurements are collected from the University NAVSTAR Consortium (http://www.unavco.org/data/gps-gnss/gps-gnss.html) and used for studying seismic-ionospheric perturbations following the 2005 Northern California earthquake (see Figure 1), which are all located in 1,500 km far from the epicenter (41.2°N, 126.0°W). The sampling interval for all GPS stations observations is 15 or 30 s. Using these dense GPS observations, the highly temporal-spatial seismic ionospheric perturbations can be estimated from the filtered TEC series. In the following sections, the seismic-ionospheric disturbance pattern and modes are investigated and discussed.

3. Results and Discussion

3.1. Coseismic Ionospheric Disturbances

The ionospheric responses and disturbances following the 2005 Northern California offshore earthquake are obtained and analyzed using GPS TEC time series. Figure 2 shows the filtered TEC maps from 03:00 UT to 03:09 UT with a time interval of 3 min. The black pentagram represents the location of the earthquake, the colorful solid dot displays the position of the subionospheric point (SIP) at a certain point, and the color values indicate the amplitude of the TEC disturbance or filtered TEC. The filtered TEC is obtained by using the Butterworth filter of the fourth-order zero-phase pulse with a 3–8-mHz window, which is to remove the ionospheric background variations and the trend of SIP's motion. The remaining TEC disturbances are mainly related to the earthquake (Tsugawa et al., 2011). After about 10 min of the main shock, the ionospheric anomalies are detected around the epicenter, and 3 min later at 03:03 UT, the anomalies became distinct. The TEC disturbances are mainly located in the south of the epicenter, and most of the disturbances appeared in a form of positive anomalies with the first appearing positive amplitudes. Then the anomalies become stronger at 03:06 UT and the TEC disturbance reaches its maximum amplitude around this time point. An obvious feature is that positive anomalies occur in the vicinity of the epicenter, while negative anomalies are far from the epicenter. The TEC amplitude decreases at 03:09 UT and the TEC anomalies become less distinct. In order to better distinguish and show seismic ionospheric perturbations, the filtered TECs of higher than 0.02 total electron content unit (TECU) or less than −0.02 TECU are displayed by the last or first value color in the color bar. It can be seen that the amplitude near the epicenter is more than 0.1 TECU. The seismic ionospheric perturbation appears near the epicenter first and then quickly spreads out to 500 km in 15 min far from the epicenter. Also, most significant ionospheric disturbances are found in the south side, while no significant ionospheric disturbances are found in the north side, which may be due to the weak ionospheric

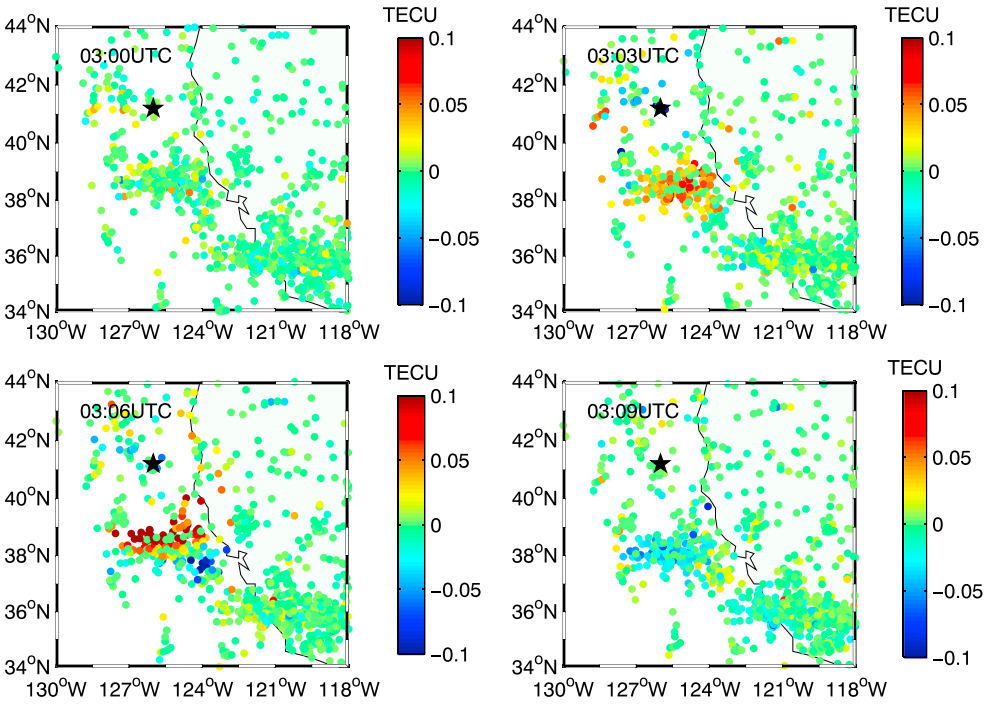

Figure 2. Two-dimensional filtered TEC maps during 03:00–03:09UT (universal time). The pentagram shows the location of the epicenter and the colorful solid dot presents the position of the SIP. The filtered TEC amplitudes are colored using the color maps presented at the right.

disturbances or lower solid-Earth and ionospheric coupling in the north side. This is also contributing to the northern attenuation observed in the TEC pattern from satellite 24 (Heki & Ping, 2005). In addition, the local geomagnetic field in the north side may cause insignificant ionospheric disturbances. We estimate the ionospheric coupling factor using a radial wave vector with 10° zenith angle (Rolland et al., 2011). The ionospheric coupling factor shows that the ionospheric coupled wave is more attenuated in the north than in the south, indicating the southeastward directivity and the lack of signal in the north at near field (Afraimovich et al., 2010). However, it is still complex for the north-south anisotropy, which is mostly related to the combination of three factors: the seismic source, the geomagnetic field, and the observation geometry. In the future, it needs to further study with more real observations, particularly effect of nonuniform observation geometry of GPS stations (Occhipinti et al., 2008, 2013).

Figure 3 shows detailed features of TEC anomalies detected from PRN10. The left of the top panel displays the SIP traces of each GPS station from 02:30 to 04:00 (UT), the blue dot represents the location of SIPs when the earthquake occurred, the dashed red curve shows the trace of SIPs, and the black pentagram is the epicenter. The distributions of SIP tracks are mainly located in the south of the epicenter with traveling from the north to the south during the selected period. The right of the top panel displays the average filtered TEC in TECU with the distance, and the average amplitude is calculated from all the cases except that the amplitude is less than 0.04 TECU. The maximum of the average filtered TEC for each range appeared near 03:00 UT and the amplitude of average filtered TEC anomalies decreased with the distance away from the epicenter. The bottom panel displays the travel time diagram for PRN08 and PRN10. The fitting speed from this diagram is 2.31 km/s.

Figure 4 shows ionospheric piercing point tracks at station P267 with PRN08 (a) and HOTK with PRN10 (b) from 02:30 to 04:00 UT, filtered TEC time series, the elevation angle, and distance changes. The top panel is the SIP trace from UT 02:30 to 04:00 UT, the black pentagram represents the epicenter, and the red triangle displays the location of station P267 and HOTK. The elevation angle (in blue line) and the distance (in yellow line) between the epicenter and SIPs are also presented in the bottom panel. The TEC anomalies are clearly observed after about 12 min of the main shock in the form of an inverted *N* shape. The smaller amplitude with about 0.04 TECU is found for station P267 and satellite 08 in the left panel with the elevation angle range of 40–80°, while the larger amplitude around 0.10 TECU is found for station HOTK and satellite 10 in the right

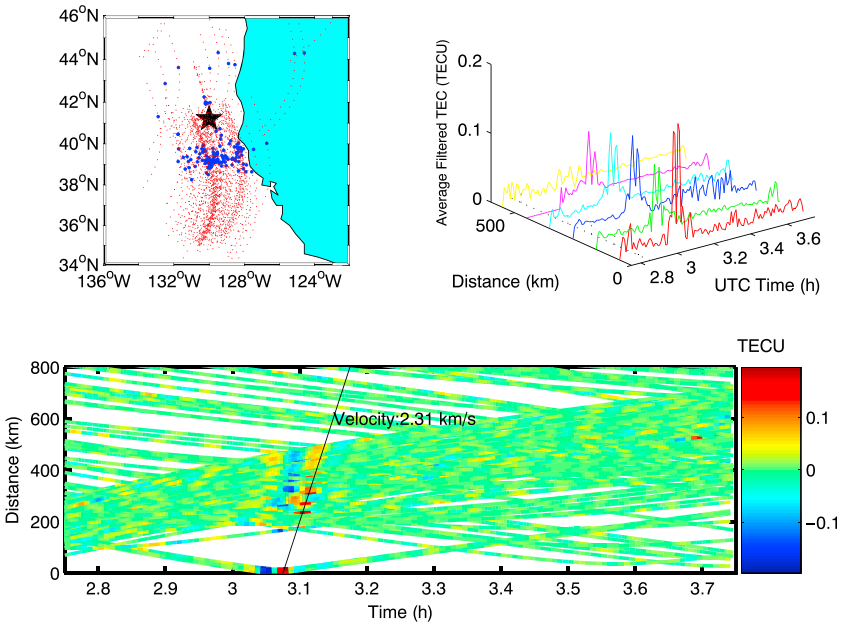

Figure 3. Travel time diagram of seismic ionospheric disturbance following the M_w = 7.2 Northern California earthquake for GPS PRN10 satellite (bottom panel). The left of the top panel shows the SIP traces of each GPS station from 02:30 to 04:00 (UT), the blue dot represents the location of SIPs when the earthquake occurred, and the dashed red curve shows the trace of SIPs. The right of the top panel displays the average filtered TEC with the distance.

panel with the elevation angle range of 15–25°. The GPS TEC observation with lower elevation angle is sensitive to coseismic ionospheric disturbances induced by Rayleigh waves (e.g., Jin, Jin, & Li, 2017).

3.2. Two-Mode Disturbances

The seismic ionospheric disturbances with the travel time and the epicentral distance have clear linear relationship, which may indicate different SID characteristics and sources. In order to know seismic ionospheric perturbation patterns and modes, the SID velocities following the 2005 Northern California offshore earthquake are estimated and investigated from the filtered TEC perturbation time series at different ionospheric pierce points. Here the propagation speeds of seismic ionospheric perturbations are obtained using the linear fitting with the epicentral distance of the ionospheric TEC disturbance at maximum amplitudes following the time delay. Figure 5 shows the traveling graphs of filtered TEC time series following this earthquake for GPS PRN10 and PRN08 satellites. Two linear relationships between the SID travel time and epicentral distance are clearly seen. Two significantly distinguished ionospheric perturbation modes are found following this earthquake. One is the slow seismic ionospheric perturbation that is spreading at 1.51 km/s, and the other is the fast seismic ionospheric perturbation at 2.31 km/s. Such ionospheric TEC perturbations are probably generated by the acoustic waves with velocity 500–1,500 m/s and Rayleigh waves with velocity 2,000–4,000 m/s due to dynamic coupling.

The slow mode SID speed with 1.51 km/s is nearly similar to the acoustic velocity of about 1 km/s at 300–500-km height. The significant slow mode propagating perturbations are observed from nearby epicenter to 800 km away and reaches the first peak after 9.5 min of the earthquake, while the 9.5 min are close to the time of a pulse disturbance that propagate to the ionospheric level. Therefore, the slow-propagating mode of seismic ionospheric disturbances is the acoustic wave spreading at the height of the ionosphere, which is caused by the fault dislocation near the earthquake rupturing region.

The fast mode of seismic ionospheric perturbations is significantly found in 10–20 min after this earthquake from the epicenter to 500 km away, whose velocity is 2.31 km/s. The fast-propagating mode signal has normally superimposed on the slow-propagating mode, which will separate with the increase of the epicentral distance (Astafyeva & Heki, 2009). The fast and slow modes have the similar time delay after the earthquake, and therefore, the upward propagation of the two-mode ionospheric disturbances should be the same. However, the fast mode propagating speed is close to that of the seismic Rayleigh wave propagation, but

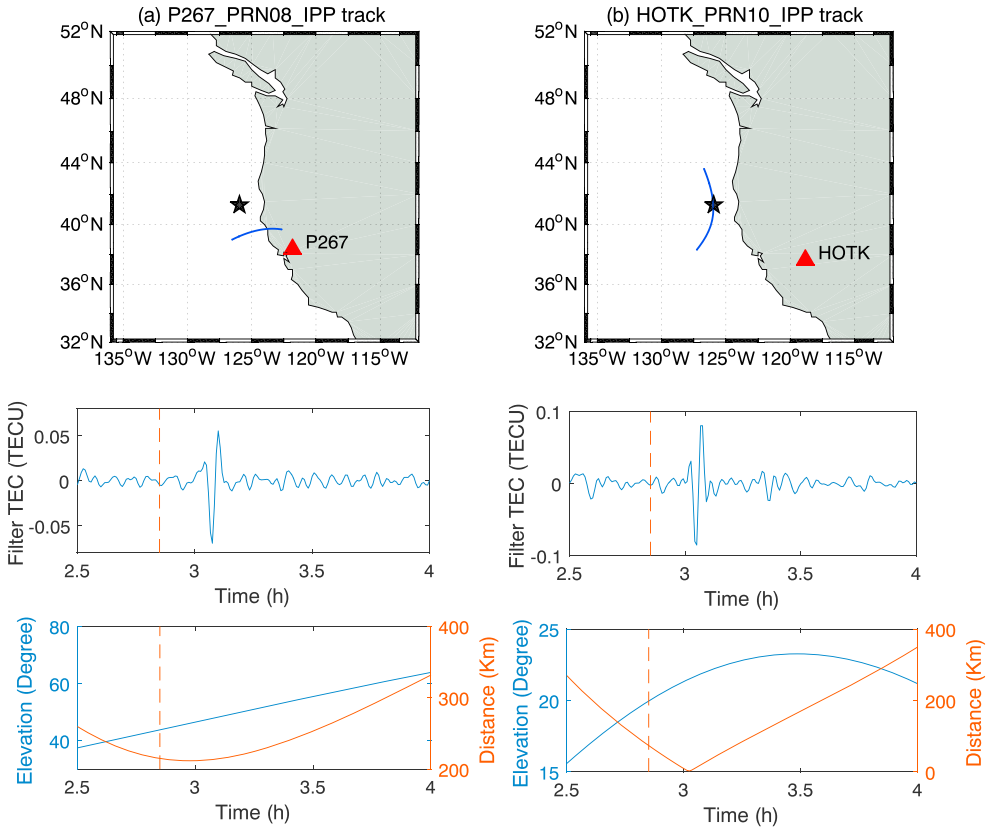

Figure 4. IPP tracks at (a) station P267 with PRN08 and (b) HOTK with PRN10 from 02:30 to 04:00, filtered TEC time series, the elevation angle, and distance changes.

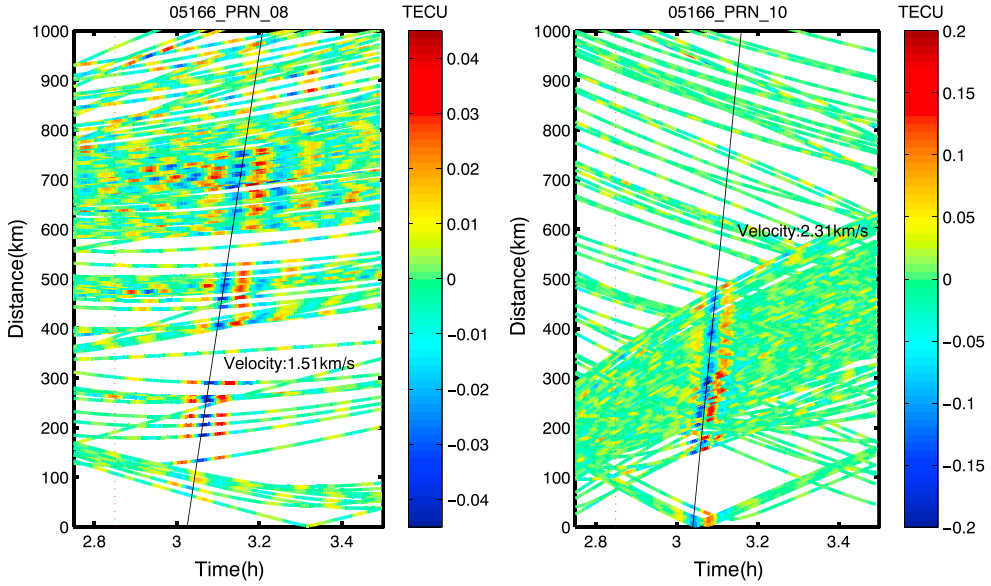

Figure 5. Travel time diagrams of seismic ionospheric disturbance following the M_w = 7.2 Northern California earthquake for GPS PRN08 and 10 satellites. The horizontal axis represents the time from the beginning of the earthquake, that is, 02:50:54 UT. The vertical axis represents the epicentral distance. Colors show the disturbance amplitudes extracted from GPS TEC series with Butterworth band-pass filter. The blue line is the first-order fitting line for the first-peak disturbance.

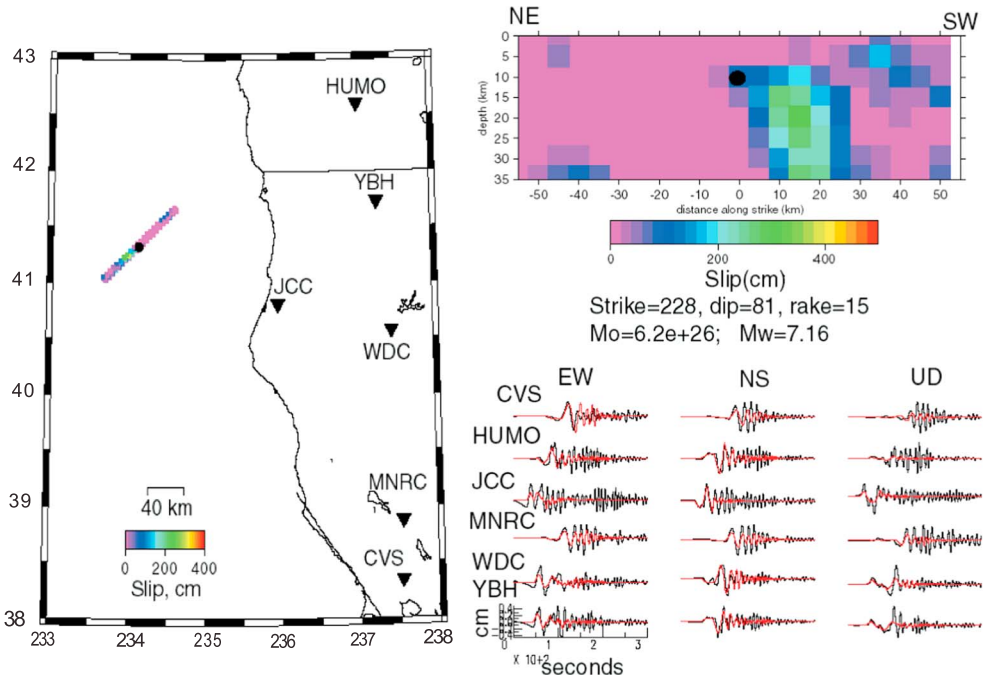

Figure 6. Slip map for the 2005 M_w = 7.2 earthquake from California Integrated Seismic Network.

faster than the acoustic velocity at the ionospheric height. Therefore, the fast-propagating mode of ionospheric disturbances is more probably the up propagating secondary acoustic wave, which is induced by the seismic Rayleigh wave. Also, the fast-propagating Rayleigh wave disturbance and the slow-propagating acoustic wave disturbance are very clear within 500 km far from the epicenter. After about 500 km, the amplitudes of seismic ionospheric disturbances due to seismic Rayleigh wave and the acoustic wave decrease gradually with the decay of earthquake energy release.

In addition, the significant fast and slow mode SIDs are mainly located in the southeast of the epicenter (Figures 2 and 5), particularly at the direction of about epicentral azimuth 140–220°. Figure 6 shows the slip map of the 2005 M_w = 7.2 NC earthquake from California Integrated Seismic Network (http://www.cisn.org/special/evt.05.06.15). The slip solution matches the northeast-southwest trending fault plane with strike of 228°, which is consistent with the historic earthquake events and the distribution of the larger aftershocks in the Gorda plate. The slip appears to be unilateral with larger rupture in the SW. The seismo-ionospheric disturbances are almost parallel to the fault plane with large anomalies in the south, which is consistent with large ruptures of that region. Furthermore, the fast mode is observed at the elevation angles 15–25° of corresponding line of sight (LOS), while the slow mode is observed at the elevation angles 45–50° of corresponding line of sight (LOS) (Figure 7). As the GPS-TEC is affected by lots of factors, GPS TEC time series are most sensitive to the perpendicular disturbances along the LOS. The fast mode of seismic ionospheric perturbations is the up propagating secondary acoustic wave triggered by the Rayleigh wave, so the low-elevation angle LOS TEC is more sensitive to vertical ionospheric disturbance. Since the slow mode ionospheric disturbance is propagating horizontally as the acoustic wave, the high-elevation angle LOS TEC is sensitive to horizontal ionospheric disturbance. Therefore, the fast mode is observed at the lower elevation angles of corresponding line of sight (LOS), while the slow mode is observed at the higher-elevation angles of corresponding line of sight (LOS). The distributions of the GPS PRN10 and PRN08 elevation angles provide good observation geometry to distinguish the horizontal and vertical acoustic wave propagations. Therefore, the two modes of seismic ionospheric perturbations are clearly observed and distinguished in near-field GPS observations following the 2005 Northern California offshore earthquake. Unlike the 2004 M_w = 9.0 Sumatra-Andaman earthquake and the 2011 M_w = 9.1 Tohoku-Oki earthquake, a smaller magnitude and ground uplift occurred for this strike-slip earthquake. The seismic ionospheric effect is more similar to a point source disturbance, which makes the two modes highly distinguishable in the near field. The distance distribution also has much difference between the fast mode and the slow mode. Figure 8 shows the distance

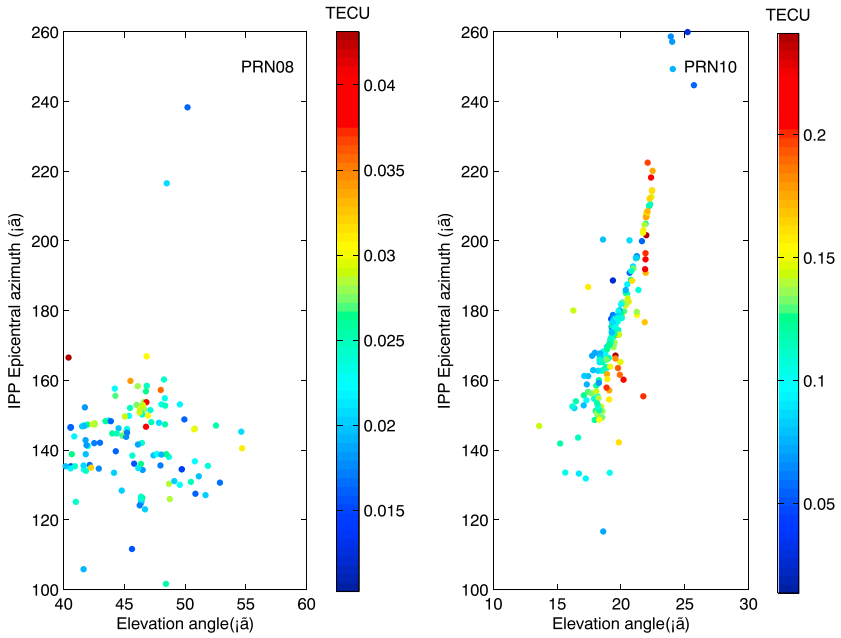

Figure 7. IPP epicentral azimuth and corresponding LOS satellite elevation angle distribution for maximum filtered TEC in each GPS observation arc. Here the undisturbed arcs (maximum filtered TEC <0.01 TECU) are not considered.

distribution of the maximum filtered TEC of each time series for the fast and slow modes, respectively. The red triangles represent the fast mode and the blue circles represent the slow mode. The maximum amplitude of the fast mode filtered TEC time series is much bigger than that of the slow mode. And most cases of the fast mode have a maximum amplitude larger than 0.04 TECU while most amplitudes of the slow mode are less than 0.04 TECU. In addition, the significant fast mode seismo-ionospheric disturbances are less in the range of 500–600 km away from the epicenter, while the slow mode ionospheric disturbances are still significant with more than 600 km far from the epicenter. The fast mode is the up propagating secondary acoustic wave triggered by the Rayleigh wave, so the seismo-ionospheric disturbance ranges are smaller. The slow mode is propagating horizontally as the acoustic wave, which has larger range effects.

3.3. Waveform and Spectral Analysis

The distinct TEC disturbances are detected after the earthquake with PRN08 and PRN10. Figure 9 presents 10 cases of each satellite to show the feature of the TEC anomalies. The left panel is for PRN08 and the right panel is for PRN10. The red dotted line shows the location of the main shock, and the station name of each selected cases is located in the right of each panel. The significant TEC disturbances appear after about 10 min of the main shock, and for most selected cases, the anomalies last less than 15 min. The ionospheric anomalies appear in the form of an inverted *N* shape instead of an typical *N* shape, indicating that the first TEC disturbances are negative anomalies instead of positive anomalies. The polarity of the ionospheric anomalies is closely related to the mechanism and earthquake process.

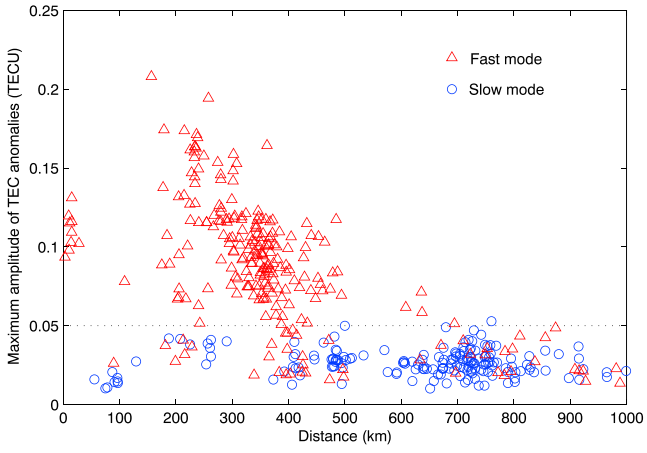

Figure 8. The distance distribution of the maximum filtered TEC of each time series for the fast and slow modes.

Based on previous findings (Afraimovich et al., 2010), the typical polarity distribution of anomalies is often found following the reverse motion earthquakes or normal motion earthquakes. These two types of earthquakes generate vertical coseismic crustal displacement. For most cases, the normal motion mainly causes subsidence of the surface, while the reverse motion causes uplift of the surface. For example, Astafyeva and Heki (2009) found both regular *N* waves and inverted *N* waves after the 4 October 1994 earthquake. The *N* waves (positive changes) appeared in the southeast of the epicenter above the uplifted area, while the

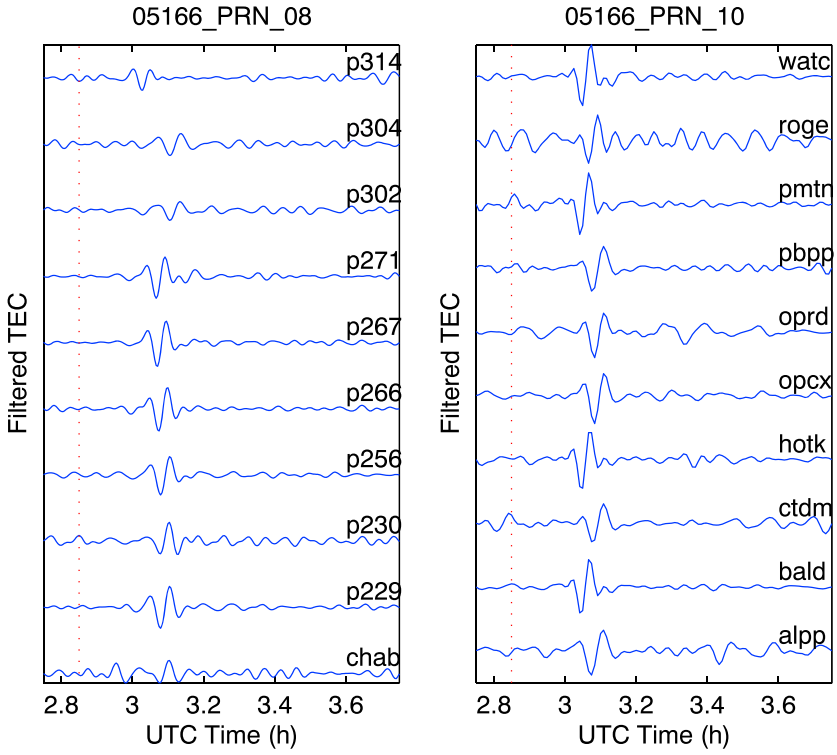

Figure 9. Filtered TEC time series after the earthquake.

inverted *N* waves (negative changes) appeared northwest of the epicenter above the area of subsidence. The type of the 2005 Northern California offshore earthquake was strike-slip motion earthquake, and the crustal displacement was mainly in the horizontal direction. Figure 10 shows the polarity distribution of the perturbations, and the red triangles and the blue dots represent the negative TEC change and positive TEC change, respectively. The major ionospheric anomalies are located in the south of the epicenter in the form of the negative changes. The polarities of ionospheric disturbances with less positive and more negative spreading are probably due to high and low acoustic wave velocities of the compression and rarefactions, respectively. The polarities of ionospheric disturbances may reflect coseismic vertical crustal movements (i.e., uplift or subsidence). The negative changes are located in the subsidence areas, indicating that the ground subsidence induces coseismic ionosphere disturbances starting with negative changes (Astafyeva & Heki, 2009). Therefore, the coseismic ionospheric disturbances may provide a potential of information on focal processes of earthquakes. However, there remain several physical problems in the formation and propagation of the inverted *N*-type waves, that is, other geomagnetic field effect (Sunil et al., 2017).

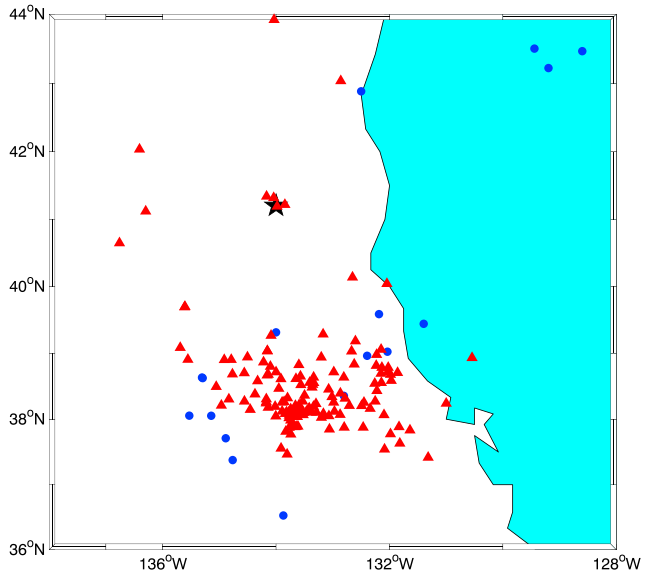

Figure 10. The polarity distribution of seismo-ionospheric perturbations. The red triangles represent the negative anomalies, and the blue dots represent the positive anomalies.

Figure 11 shows the spectrograms of filtered TEC time series for selected stations and satellites. From up to bottom are PRN08 for station CHAB and station P304, PRN10 for station BALD and station ROGE. The left panel shows the filtered TEC time series in blue and distance time series in green, respectively, and the right panel displays the spectrograms of the corresponding cases. The frequency is centered at about 3.7 mHz for CHAB and P304, which is case of the slow speed mode, while the frequency centered at about 5.6 mHz for BALD and ROGE is case of the fast mode. The frequencies are all in the range of the infrasonic wave.

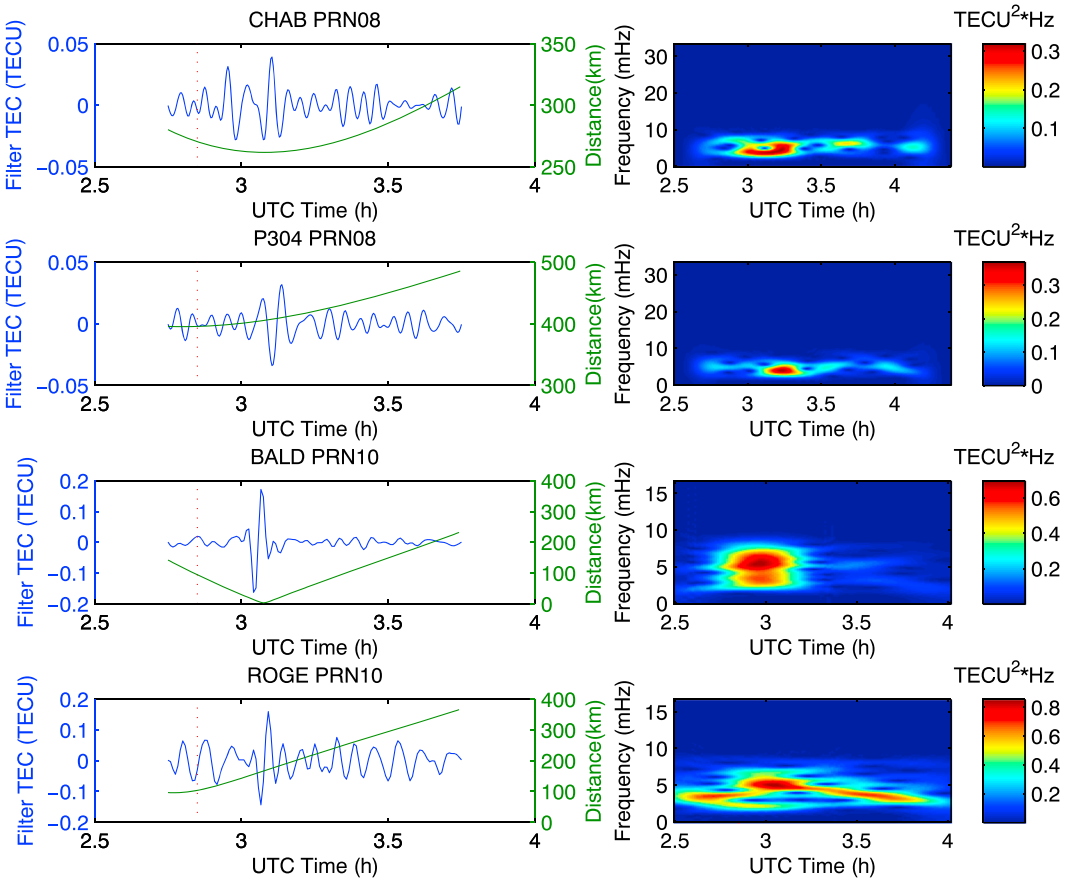

Figure 11. Spectrograms for station CHAB of satellite PRN08, station P304 of satellite PRN08, station BALD of satellite PRN10, and station ROGE of satellite PRN10. The left panel displays the filtered TEC time series in blue and the distances between the volcano and the IPP of corresponding stations and satellites in green.

3.4. Discussion

GPS-TEC is used to detect the ionospheric anomalies following the 2005 Northern California offshore earthquake. The significant TEC disturbances are detected after about 10 min of the main shock. The maximum amplitude of the filtered TEC time series is around 0.2 TECU and generally the amplitude decreases with the distance between the epicenter and the SIPs. The ionospheric anomalies are mainly located in the south of the epicenter and lasts for less than half an hour for most cases. The distinct TEC disturbances are detected from satellite PRN08 and satellite PRN10 and two seismo-ionospheric disturbance modes are found. Furthermore, two modes are compared in the velocity, amplitude, elevation angle or azimuth, and frequency. The TEC anomalies detected from satellite PRN08 travel at a propagating speed of 1.51 km/s, while the TEC anomalies from PRN10 are spreading at a velocity of around 2.31 km/s. The slow mode has an amplitude of 0.02–0.04 TECU, while the fast mode has a larger amplitude of 0.1–0.2 TECU. The most dramatic ionospheric disturbances are located at about 140° of epicentral azimuth, while the elevation angle is different for corresponding line of sight (LOS). The elevation angles of LOS are 45–50° for the observed slow mode and about 15–25° for the fast mode, respectively.

The 2005 Northern California offshore earthquake was a result of strike-slip motion. According to our findings, the strike-slip earthquake can also trigger the ionospheric anomalies detected by GPS-TEC. The detected fast mode and slow mode indicated that strike-slip earthquakes can cause different types of ionospheric disturbances. Although unlike reverse motion earthquakes or normal motion earthquakes, there was less vertical crustal displacement with about 2 m, but the typical polarity distribution of the ionospheric perturbations are found (e.g., Astafyeva & Heki, 2009).

As GPS satellites are moving and ground GPS stations are limited, the observation geometry of GPS plays a vital part in detecting seismic ionospheric anomalies. The seismic ionospheric disturbance modes can be observed from continuous GPS TEC time series. However, the observation geometry of GPS is not uniform, which may affect SID estimations. To better understand seismo-ionospheric perturbation characteristics and evolution, a more accurate morphology of ionospheric disturbances following the earthquakes should be further investigated with more GPS observations. With the rapid development of more and more GNSS constellations, for example, China's BeiDou and updating Russia's GLONASS as well as European Union's Galileo, it will provide more chances to study and understand seismo-ionospheric perturbations in the future, including effects of the GNSS observation geometry on SID.

4. Summary

In this paper, significant ionospheric disturbances following the 2005 Northern California offshore earthquake are observed about 10 min after the onset by denser GPS measurements with 504 stations. Two clear propagating modes of seismic ionospheric disturbances are found, namely, the fast-propagating mode with a speed of 2.31 km/s and the slow-propagating mode with a speed of 1.51 km/s. The fast mode of ionospheric disturbances is detected in the range of less than 500–600 km away from the epicenter, while the slow mode of ionospheric disturbances is found more than 600 km far from the epicenter during 10–20 min. The maximum amplitude of the fast mode TEC disturbances is much bigger than that of the slow mode. Most cases of the fast mode have a maximum amplitude larger than 0.04 TECU, while most amplitudes of the slow mode are less than 0.04 TECU. Furthermore, the frequency spectrogram of the slow-propagating mode is around 3.7 mHz, while typical frequency of the fast-propagating mode is about 5.3 mHz. In addition, the seismic ionospheric disturbances are much stronger in the southeast when compared to the northwest. The fast-propagating mode of ionospheric perturbations is the up propagating secondary acoustic wave induced by the seismic Rayleigh wave, while the slow-propagating mode of ionospheric disturbances is the horizontal acoustic wave induced by the focal dislocation.

Acknowledgments
This work was supported by the Startup Foundation for Introducing Talent of NUIST (grant 2243141801036) and National Natural Science Foundation of China (NSFC) Project (grants 11573052 and 41761134092). The author also thanks Rui Jin and Xin Liu for the experimental tests and assistance as well as UNAVCO for providing the GPS data (http://www.unavco.org/data/gps-gnss/gps-gnss.html).

References

Afraimovich, E. L., Astafyeva, E. I., Demyanov, V. V., Edemskiy, I. K., Gavrilyuk, N. S., Ishin, A. B., et al. (2013). A review of GPS/GLONASS studies of the ionospheric response to natural and anthropogenic processes and phenomena. *Journal of Space Weather & Space Climate*, *3*, A27. https://doi.org/10.1051/swsc/2013049

Afraimovich, E. L., Ding, F., Kiryushkin, V. V., Astafyeva, E., Jin, S. G., & San'kov, V. (2010). TEC response to the 2008 Wenchuan earthquake in comparison with other strong earthquakes. *International Journal of Remote Sensing*, *31*(13), 3601–3613. https://doi.org/10.1080/01431161003727747

Aoyama, T., Iyemori, T., Nakanishi, K., Nishioka, M., Rosales, D., Veliz, O., & Safor, E. V. (2016). Localized field-aligned currents and 4-min TEC and ground magnetic oscillations during the 2015 eruption of Chile's Calbuco volcano. *Earth, Planets and Space*, *68*(1), 148. https://doi.org/10.1186/s40623-016-0523-0

Astafyeva, E., & Heki, K. (2009). Dependence of waveform of near-field coseismic ionospheric disturbances on focal mechanisms. *Earth, Planets and Space*, *61*(7), 939–943. https://doi.org/10.1186/BF03353206

Astafyeva, E., Rolland, L. M., & Sladen, A. (2014). Strike-slip earthquakes can also be detected in the ionosphere. *Earth and Planetary Science Letters*, *405*, 180–193. https://doi.org/10.1016/j.epsl.2014.08.024

Blewitt, G. (1990). An automatic editing algorithm for GPS data. *Geophysical Research Letters*, *17*(3), 199–202. https://doi.org/10.1029/GL017i003p00199

Brunini, C., & Azpilicueta, F. J. (2009). Accuracy assessment of the GPS-based slant total electron content. *Journal of Geodesy*, *83*(8), 773–785. https://doi.org/10.1007/s00190-008-0296-8

Calais, E., & Minster, J. B. (1995). GPS detection of ionospheric perturbations following the January 17, 1994, Northridge earthquake. *Geophysical Research Letters*, *22*(9), 1045–1048. https://doi.org/10.1029/95GL00168

Catherine, J. K., Maheshwari, D. U., Gahalaut, V. K., Roy, P. N. S., Khan, P. K., & Puviarasan, N. (2017). Ionospheric disturbances triggered by the 25 April 2015 *M*7.8 Gorkha earthquake, Nepal: Constraints from GPS TEC measurements. *Journal of Asian Earth Sciences*, *133*, 80–88. https://doi.org/10.1016/j.jseaes.2016.07.014

Dautermann, T., Calais, E., & Mattioli, G. S. (2009). Global positioning system detection and energy estimation of the ionospheric wave caused by the 13 July 2003 explosion of the Soufrière Hills volcano, Montserrat. *Journal of Geophysical Research*, *114*, B02202. https://doi.org/10.1029/2008JB005722

Grawe, M. A., & Makela, J. J. (2016). The ionospheric responses to the 2011 Tohoku, 2012 Haida Gwaii, and 2010 Chile tsunamis: Effects of tsunami orientation and observation geometry. *Earth & Space Science*, *2*(11), 472–483.

Heki, K., Otsuka, Y., Choosakul, N., Hemmakorn, N., Komolmis, T., & Maruyama, T. (2006). Detection of ruptures of Andaman fault segments in the 2004 great Sumatra earthquake with coseismic ionospheric disturbances. *Journal of Geophysical Research*, *111*, B09313. https://doi.org/10.1029/2005JB004202

Heki, K., & Ping, J. (2005). Directivity and apparent velocity of the coseismic ionospheric disturbances observed with a dense GPS array. *Earth and Planetary Science Letters*, *236*(3-4), 845–855. https://doi.org/10.1016/j.epsl.2005.06.010

Jin, S. G., Cho, J., & Park, J. (2007). Ionospheric slab thickness and its seasonal variations observed by GPS. *Journal of Atmospheric and Solar-Terrestrial Physics*, *69*(15), 1864–1870. https://doi.org/10.1016/j.jastp.2007.07.008

Jin, S. G., Han, L., & Cho, J. (2011). Lower atmospheric anomalies following the 2008 Wenchuan earthquake observed by GPS measurements. *Journal of Atmospheric and Solar-Terrestrial Physics*, *73*(7–8), 810–814. https://doi.org/10.1016/j.jastp.2011.01.023

Jin, S. G., Jin, R., & Kutoglu, H. (2017). Positive and negative ionospheric responses to the March 2015 geomagnetic storm from BDS observations. *Journal of Geodesy*, *91*(6), 613–626. https://doi.org/10.1007/s00190-016-0988-4

Jin, S. G., Jin, R., & Li, D. (2016). Assessment of BeiDou differential code bias variations from multi-GNSS network observations. *Annales de Geophysique*, *34*(2), 259–269. https://doi.org/10.5194/angeo-34-259-2016

Jin, S. G., Jin, R., & Li, D. (2017). GPS detection of ionospheric Rayleigh wave and its source following the 2012 Haida Gwaii earthquake. *Journal of Geophysical Research: Space Physics*, *122*, 1360–1372. https://doi.org/10.1002/2016JA023727

Jin, S. G., Jin, R., & Li, J. H. (2014). Pattern and evolution of seismo-ionospheric disturbances following the 2011 Tohoku earthquakes from GPS observations. *Journal of Geophysical Research: Space Physics*, *119*, 7914–7927. https://doi.org/10.1002/2014JA019825

Jin, S. G., Occhipinti, G., & Jin, R. (2015). GNSS ionospheric seismology: Recent observation evidences and characteristics. *Earth-Science Reviews*, *147*, 54–64. https://doi.org/10.1016/j.earscirev.2015.05.003

Jin, S. G., Park, J., Wang, J., Choi, B., & Park, P. (2006). Electron density profiles derived from ground-based GPS observations. *Journal of Navigation*, *59*(3), 395–401. https://doi.org/10.1017/S0373463306003821

Jin, S. G., & Park, J. U. (2007). GPS ionospheric tomography: A comparison with the IRI-2001 model over South Korea. *Earth, Planets and Space*, *59*(4), 287–292. https://doi.org/10.1186/BF03353106

Jin, S. G., Wang, J., Zhang, H., & Zhu, W. Y. (2004). Real-time monitoring and prediction of the total ionospheric electron content by means of GPS observations. *Chinese Astronomy and Astrophysics*, *28*(3), 331–337. https://doi.org/10.1016/j.chinastron.2004.07.008

Liu, J. Y., Tsai, Y. B., Chen, S. W., Lee, C. P., Chen, Y. C., Yen, H. Y., et al. (2006). Giant ionospheric disturbances excited by the *M*9.3 Sumatra earthquake of 26 December 2004. *Geophysical Research Letters*, *33*, L02103. https://doi.org/10.1029/2005GL023963

Occhipinti, G., Kherani, E. A., & Lognonné, P. (2008). Geomagnetic dependence of ionospheric disturbances induced by tsunamigenic internal gravity waves. *Geophysical Journal International*, *173*(3), 753–765. https://doi.org/10.1111/j.1365-246X.2008.03760.x

Occhipinti, G., Rolland, L., Lognonné, P., & Watada, S. (2013). From Sumatra 2004 to Tohoku-oki 2011: The systematic GPS detection of the ionospheric signature induced by tsunamigenic earthquakes. *Journal of Geophysical Research: Space Physics*, *118*, 3626–3636. https://doi.org/10.1002/jgra.50322

Rolland, L. M., Lognonné, P., & Munekane, H. (2011). Detection and modeling of Rayleigh wave induced patterns in the ionosphere. *Journal of Geophysical Research*, *116*, A05320. https://doi.org/10.1029/2010JA016060

Rolland, L. M., Vergnolle, M., Nocquet, J. M., Sladen, A., Dessa, J. X., Tavakoli, F., et al. (2013). Discriminating the tectonic and non-tectonic contributions in the ionospheric signature of the 2011, M_w 7.1, dip-slip van earthquake, eastern Turkey. *Geophysical Research Letters*, *40*, 2518–2522. https://doi.org/10.1002/grl.50544

Saito, A., Tsugawa, T., Otsuka, Y., Nishioka, M., Iyemori, T., Matsumura, M., et al. (2011). Acoustic resonance and plasma depletion detected by GPS total electron content observation after the 2011 off the Pacific coast of Tohoku earthquake. *Earth, Planets and Space*, *63*(7), 863–867. https://doi.org/10.5047/eps.2011.06.034

Shinagawa, H., Iyemori, T., Saito, S., & Maruyama, T. (2007). A numerical simulation of ionospheric and atmospheric variations associated with the Sumatra earthquake on December 26, 2004. *Earth, Planets and Space*, *59*(9), 1015–1026. https://doi.org/10.1186/BF03352042

Sunil, A. S., Bagiya, M. S., Catherine, J., Rolland, L., Sharma, N., Sunil, P. S., & Ramesh, D. S. (2017). Dependence of near field co-seismic ionospheric perturbations on surface deformations: A case study based on the April, 25 2015 Gorkha Nepal earthquake. *Advances in Space Research*, *59*(5), 1200–1208. https://doi.org/10.1016/j.asr.2016.11.041

Tsugawa, T., Saito, A., Otsuka, Y., Nishioka, M., Maruyama, T., Shinagawa, H., et al. (2011). Ionospheric disturbances detected by GPS total electron content observation after the 2011 Tohoku earthquake, AGU Fall Meeting. AGU Fall Meeting Abstracts.

Vukovic, J., & Kos, T. (2017). Locally adapted NeQuick 2 model performance in European middle latitude ionosphere under different solar, geomagnetic and seasonal conditions. *Advances in Space Research*, *60*(8), 1739–1750. https://doi.org/10.1016/j.asr.2017.05.007